Title

Bismuth-assisted low-temperature growth of flexible GaSb thin films by multi-cathode RF magnetron sputtering

Author(s)

Nishimoto N and Fujihara J.

Journal

J Mater Sci 2023:58;11174–11186

Published

2023

URL（The Version of Record）

https://doi.org/10.1007/s10853-023-08735-6

Bismuth-assisted low-temperature growth of flexible GaSb thin films by multi-cathode RF magnetron sputtering

Naoki Nishimoto[1,*], Junko Fujihara[2]

[1] Department of Research Planning and Coordination, Shimane Institute for Industrial Technology, 1 Hokuryo, Matsue, Shimane 690-0816, Japan

ORCID: 0000-0002-5854-7848

[2] Department of Legal Medicine, Shimane University Faculty of Medicine, 89-1 Enya, Izumo, Shimane 693-8501, Japan

ORCID: 0000-0001-5359-5181

[*] **Corresponding author:**

Naoki Nishimoto

E-mail: nishimoto.su2010@gmail.com

Abstract

GaSb-based thin films are expected to be applicable to biomedical and environmental devices requiring efficient operation in the near-infrared region. In this study, the effects of dilute Bi doping on the structural properties and chemical stability of GaSb thin films were examined. GaSb and $GaSb_{1-x}Bi_x$ (x = 0.011, 0.013, or 0.032) thin films were grown at 320 °C on quartz substrates and PI films by multi-cathode RF magnetron sputtering. The crystallinity of the GaSb/quartz was superior to that of the GaSb/PI. Bi doping improved the crystallinity of the GaSb thin films with the exception of $GaSb_{0.968}Bi_{0.032}$/quartz, for which the crystallinity deteriorated owing to abnormal growth due to Bi cluster formation. In addition, the crystallinity of $GaSb_{1-x}Bi_x$/PI was drastically improved at x = 0.032. The increases in grain size and hole concentration caused by Bi doping indicate that Bi assists the growth of GaSb thin films. Furthermore, elution tests revealed that Bi doping suppresses the elution of highly toxic Sb under simulated physiological conditions. These findings have the possibility to hasten the development of flexible GaSb-based biomedical and environmental devices with improved safety and lower environmental burden.

Keywords

Sputtering; GaSbBi; Bi cluster; Chemical stability

Introduction

GaSb is a III-V compound semiconductor with a relatively narrow direct band gap [1]. Because the band gap energy (ca. 0.7 eV) affords efficient device operation in the infrared (IR) region, GaSb-based materials have been applied to IR optical devices such as light-emitting diodes, laser diodes, and detectors [2, 3]. In recent years, research into GaSb-based materials has spanned from the fundamental physical properties to device applications [4–7]. Furthermore, GaSb-based devices are anticipated to be applicable to biomedical sensors because near-IR (NIR) easily transmits through biological tissues [8]. For these applications, miniaturization and energy-efficient devices are essential.

Miniaturization and energy efficiency can also be achieved for flexible devices. However, flexible devices are fabricated on flexible substrates with low heat resistance such as plastic. In the case of thin-film growth on plastic substrates, polycrystallization of the thin film is unavoidable [9, 10]. In addition, further deterioration in the crystallinity of GaSb thin films is to be expected during low-temperature growth because high-quality GaSb thin films must be grown at a comparatively high temperature (~500 °C) [11, 12]. Sputtering is advantageous for low-temperature growth owing to the high energy supplied from the source material to the substrate [13]. However, in our previous study, a substrate temperature of 470 °C (corresponding to a heater temperature of 600 °C) was necessary

to suppress the structural disorder in GaSb/quartz grown by RF magnetron sputtering [14]. Although polyimide (PI) film (e.g., Kapton by DuPont Toray) has high heat resistance, its heat-resistant temperature is only 400 °C. Hence, reducing the growth temperature is essential for growing GaSb thin films on PI film.

Metal-assisted growth can improve the crystallinity and lower the growth temperature of semiconductor materials. Mulberry-like structures composed of large numbers of condensed crystal grains were formed in ZnO-MgO mixed thin films and Sn-doped ZnO thin films, where the Mg and Sn dopants acted as catalysts [15, 16]. Gougousi reported that the crystallization of HfO_2 thin films was enhanced by the surface oxide of the GaAs substrate [17]. In addition, the effects of doping with Bi on III-V compound semiconductors have been described. For example, Mohmad et al. reported that dilute Bi doping decreased the concentration of Ga- and/or As-related defects in GaAs thin films [18]. Because high-quality InSb thin films can be obtained at low temperature (<400 °C) [19, 20], we deposited InSbBi thin films on PI films and demonstrated that dilute Bi doping suppressed the structural disorder of the InSb thin films [21].

Sputtering is an inexpensive and widely used mass-production technique compared with other methods for thin-film growth. Therefore, the direct growth of GaSb thin films on flexible substrates by sputtering has important implications for the development of

flexible GaSb-based devices. To our knowledge, there have been no reports describing the growth of flexible GaSb thin films by sputtering. In this study, we deposited GaSb and dilute GaSbBi thin films on quartz substrates and PI films by multi-cathode RF magnetron sputtering. The aim of this study was to elucidate the influence of dilute Bi doping on flexible GaSb thin films by analyzing the structural properties, electrical properties, and chemical stability.

Materials and methods

Growth of GaSb and GaSbBi thin films

A multi-cathode RF magnetron sputtering system (HSR-351L, Shimadzu Industrial Systems) was used to grow GaSb and $GaSb_{1-x}Bi_x$ thin films on quartz substrates and PI films (Kapton, DuPont Toray). Reverse sputtering was first performed to clean the surfaces of the quartz substrates and PI films under room temperature and Ar atmosphere (0.3 Pa) for 10 min. The base pressure of the sputtering system was below 2.5×10^{-4} Pa. Next, GaSb and $GaSb_{1-x}Bi_x$ thin films were deposited under an Ar atmosphere (0.5 Pa) while rotating the substrate holder at 18 rpm. The heater temperature was 425 °C, corresponding to a substrate temperature of 320 °C. To prepare GaSb thin films at various growth rates, one, two, or three $Ga_{0.497}Sb_{0.503}$ targets (2-inch-diameter disk of ≥3N purity)

were used. For the growth of $GaSb_{1-x}Bi_x$ thin films with various growth rates and Bi contents x, one $Ga_{0.498}Sb_{0.472}Bi_{0.0297}$ (2-inch-diameter disk of 3N purity) and zero, one, or two $Ga_{0.497}Sb_{0.503}$ targets (2-inch-diameter disk of ≥3N purity) were used. The RF power was set at 80 W for all targets. The growth times were adjusted in accordance with the number of sputtering targets to obtain a consistent film thickness. The growth times were 30, 15, and 10 min for one, two, and three sputtering targets, respectively.

Characterization

The film composition was analyzed by X-ray fluorescence (XRF) measurements (ZSX Primus IV, Rigaku), and the film thickness was calculated from the XRF intensity using the fundamental parameter method. The electrical properties were evaluated by Hall effect measurements using the van der Pauw configuration (HL5500PC, Nanometrics). The crystal structure and structural disorders/defects were examined by microscopic Raman scattering spectroscopy with a He-Ne laser as the excitation source (JRS-SYS2000, JEOL) and X-ray diffraction (XRD) with a multilayer mirror in the incident beam line and Cu $K\alpha_1$ radiation (SmartLab XE, Rigaku). The defect structure of the thin films was observed by transmission electron microscopy (TEM; H-9500, Hitachi) operated at 200 kV. The TEM specimens were prepared by the focused ion beam lift-out

technique (NX2000, Hitachi). The film surface morphology was analyzed by dynamic-mode atomic force microscopy (AFM; NaioAFM, Nanosurf AG). The NaioAFM system was installed on an anti-vibration table (Isostage, Nanosurf AG). The grain size was determined by analyzing the XRD pattern and surface morphology. XRD pattern analysis was performed by the direct derivation method under the whole-powder-pattern fitting technique (SmartLab Studio II, Rigaku).

Elution tests

The GaSb and GaSbBi thin films grown on PI films were immersed in 0.1 M tris buffer (pH 9, 1.5 mL) to evaluate their chemical stability. After 1 day, 0.5 mL of the immersion solutions was removed and diluted with 4.5 mL of 1N HNO_3, and additional 0.1 M tris buffer (0.5 mL) was added to replenish the immersion solution. On day 2, an additional 0.5 mL of the immersion solutions was removed and diluted as described above, and the immersion experiments were ceased because all of the GaSb on the PI films had dissolved. The eluted Ga concentrations in the samples taken from the immersion solutions were determined by microwave plasma atomic emission spectrometry (MP-AES; Agilent 4200 MP-AES, Agilent Technologies). The total Sb concentrations in the eluted solutions were measured by a hydride generation-MP-AES according to our

previous study [22].

Results and discussion

Film composition and thickness

The XRF analysis results indicated that the obtained GaSb and $GaSb_{1-x}Bi_x$ thin films were nearly stoichiometric. The Bi content x varied with the number of sputtering targets used for $GaSb_{1-x}Bi_x$ thin-film growth, with x values of 0.032 (one $Ga_{0.498}Sb_{0.472}Bi_{0.0297}$ target), 0.013 (one $Ga_{0.498}Sb_{0.472}Bi_{0.0297}$ target and one $Ga_{0.497}Sb_{0.503}$ target), and 0.011 (one $Ga_{0.498}Sb_{0.472}Bi_{0.0297}$ target and two $Ga_{0.497}Sb_{0.503}$ targets). The low Bi content x in comparison to the $Ga_{0.498}Sb_{0.472}Bi_{0.0297}$ target was thought to be caused by the segregation of Bi in the sputtering target and the lower sputtering rate of Bi compared with that of Sb [23].

After adjustment of the growth time by the number of sputtering targets, the thin-film deposition amount was estimated to be 2.96×10^{-4} g/cm^2 (SD = 9.78×10^{-6}) from the XRD intensities, irrespective of the substrates and growth rates. The film thickness was 528 nm (SD = 17.6), which was calculated using the density of GaSb (5.61 g/cm^3) for both GaSb and GaSbBi thin films because of the low Bi content in $Ga_{0.498}Sb_{0.472}Bi_{0.0297}$ target. Hence, the growth rate varied with the number of sputtering targets used: the

growth rates were 17.6 nm/min for one sputtering target, 35.2 nm/min for two sputtering targets, and 52.8 nm/min for three sputtering targets.

Growth rate and Bi content dependence of XRD patterns and Raman spectra

Figure 1 shows XRD patterns of the GaSb and $GaSb_{1-x}Bi_x$ thin films grown on quartz substrates and PI films. As shown in Fig. 1a, a decrease in the (111) diffraction intensity and an increase in the (220) diffraction intensity were observed for GaSb/quartz grown at 35.2 nm/min compared with GaSb/quartz grown at 17.6 nm/min. Previously, we reported that a change in the preferred orientation from (111) to (220) originated from increasing structural disorder in the thin film [21]. The even lower diffraction intensities for GaSb/quartz grown at 52.8 nm/min indicate further deterioration of the crystallinity with increasing growth rate. In the case of $GaSb_{1-x}Bi_x$/quartz, the diffraction intensities increased at x = 0.011 and the (111) orientation became more dominant at x = 0.013 compared with GaSb/quartz deposited at the same growth rate (Fig. 1b). However, a decrease in the diffraction intensities, the formation of Bi clusters, and a shift of the diffraction peaks to lower angles (~0.05°) were observed at x = 0.032. The peak shift implies that compressive strain was applied to $GaSb_{0.968}Bi_{0.032}$/quartz, but it was not caused by the difference in thermal expansion coefficients between the thin film and

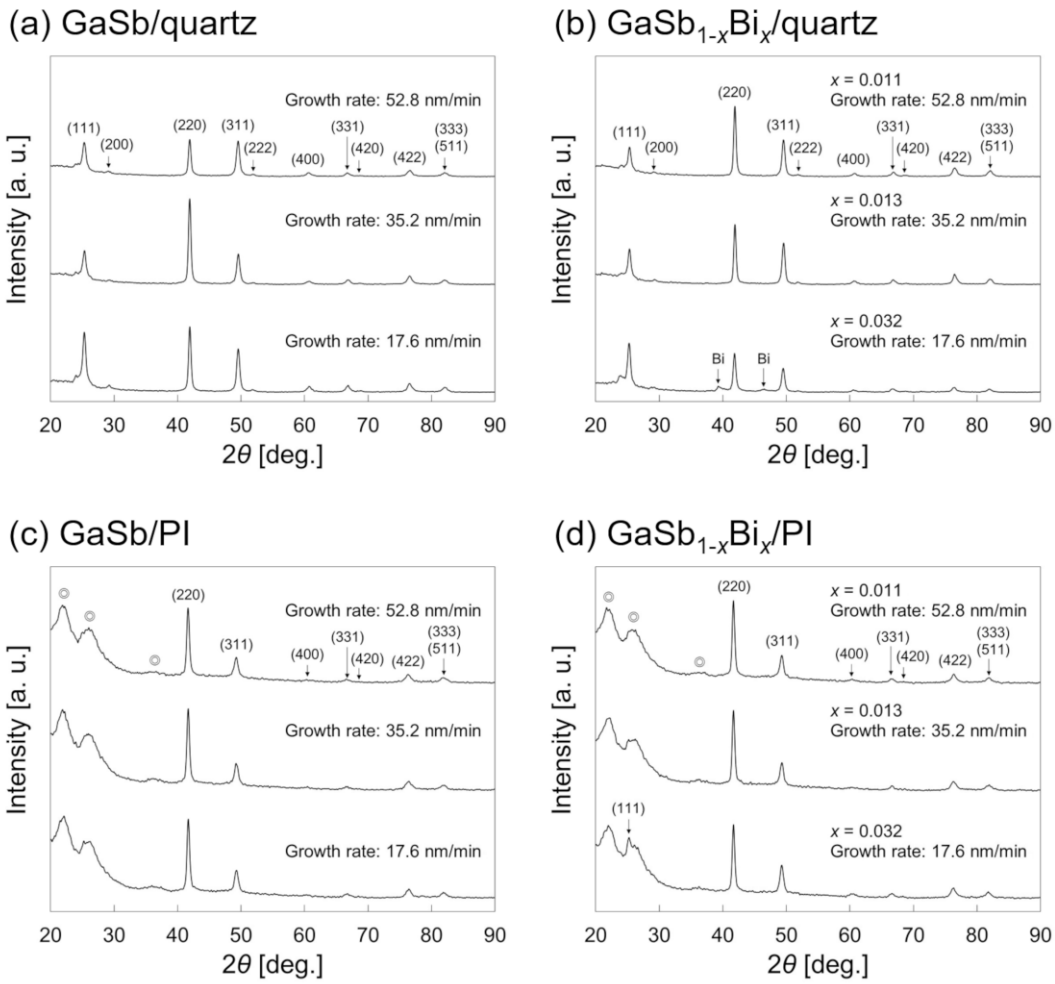

Fig. 1. XRD patterns of GaSb and $GaSb_{1-x}Bi_x$ thin films grown on quartz substrates and PI films at various growth rates and Bi contents x: (a) GaSb/quartz, (b) $GaSb_{1-x}Bi_x$/quartz, (c) GaSb/PI, and (d) $GaSb_{1-x}Bi_x$/PI. The diffraction peaks originating from the PI film appeared at approximately 22°, 26°, and 36° (double circles).

quartz substrate (7.8×10^{-6} and 5.0×10^{-7} °C^{-1} for GaSb and quartz, respectively), which would instead induce tensile strain in the thin film. On the other hand, the diffraction peaks of GaSb/PI (Fig. 1c) and $GaSb_{1-x}Bi_x$/PI (Fig. 1d) shifted to lower angles (~0.30°).

This peak shift was attributable to the difference in thermal expansion coefficients between the GaSb thin films and PI films (2.0×10^{-5} °C^{-1} for PI [24]). As shown in Fig. 1c, the XRD patterns of GaSb/PI were almost independent of the growth rate. Doping with Bi barely affected the XRD patterns of $GaSb_{1-x}Bi_x$/PI at x = 0.011 and 0.013 (Fig. 1d). However, in the XRD pattern at x = 0.032, a (111) diffraction peak appeared and the (220) diffraction intensity slightly decreased. As mentioned above, this change in the XRD patterns suggests that Bi doping improved the crystallinity of the GaSb thin films by suppressing structural disorder [21].

Raman spectroscopy was used to qualitatively evaluate the structural disorder of the GaSb and $GaSb_{1-x}Bi_x$ thin films (Figure 2). Because of the rough nature of the $GaSb_{0.968}Bi_{0.032}$/quartz surface (see the microscopy image in Fig. 2), the Raman spectra of $GaSb_{0.968}Bi_{0.032}$/quartz were measured at two positions, as indicated by (i) and (ii) in the microscopy image. The longitudinal optical (LO; green fitted curve) and transverse optical (TO; red fitted curve) modes of GaSb were observed in the Raman spectra owing to the polycrystalline thin films. According to the Raman selection rules for the zinc-blende structure, the LO mode is an allowed mode for (100) and (111), while the TO mode is an allowed mode for (110) and (111). The GaSb LO and TO modes typically appear at 236 and 226 cm^{-1}, respectively [25]. However, these modes were shifted to lower

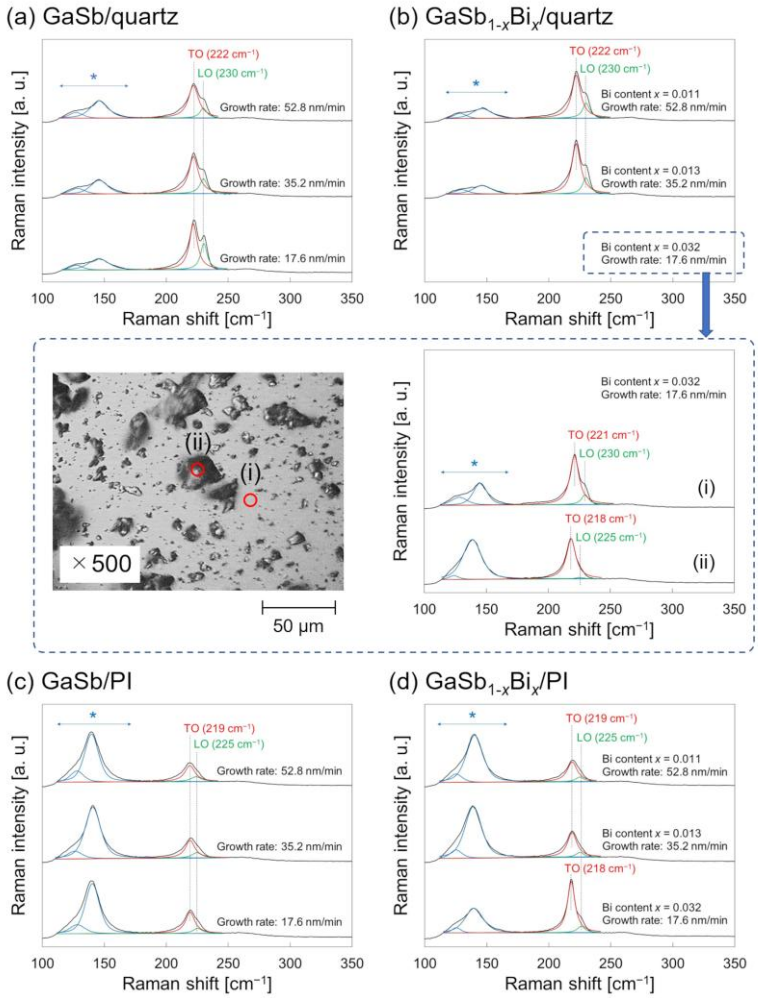

Fig. 2. Raman spectra of GaSb and $GaSb_{1-x}Bi_x$ thin films grown on quartz substrates and PI films at various growth rates and Bi contents x: (a) GaSb/quartz, (b) $GaSb_{1-x}Bi_x$/quartz, (c) GaSb/PI, and (d) $GaSb_{1-x}Bi_x$/PI. The inset microscopy image shows the surface morphology of $GaSb_{0.968}Bi_{0.032}$/quartz, and the Raman spectra of this sample were measured at the two positions labeled (i) and (ii). The green, red, and blue fitted curves represent the results of curve-fitting analysis for the peaks corresponding to the LO and TO modes of GaSb and structural disorder (region labeled *), respectively.

wavenumbers for the obtained thin films (Fig. 2). Similar Raman spectral shifts to lower

wavenumber for GaSb thin films have been described in previous studies. For example, Zhou et al. reported that the shift to lower wavenumber generated during the crystallization process by thermal treatment of the nanostructure can be explained by the phonon confinement effect [26]. Furthermore, Mishra et al. experimentally and theoretically demonstrated that the Raman peaks of Be-doped GaSb thin films with various hole concentrations become shifted as a result of plasmon damping [27]. The two peaks in the region indicated with an asterisk (*) in Fig. 2 (blue fitted curve, ~126 and ~140 cm^{-1}) originated from structural disorder of the GaSb thin film [25, 28]. Table 1 shows the results obtained from numerical analysis of the Raman spectra by curve fitting. In addition to the full width at half maximum (FWHM) values of the LO and TO modes of GaSb, the values of $(I_{\mathrm{LO}} + I_{\mathrm{TO}})/I_*$ are presented, where I_{LO} is the intensity of the GaSb LO mode, I_{TO} is the intensity of the GaSb TO mode, and I_* is the sum of the two peak intensities originating from structural disorder. $(I_{\mathrm{LO}} + I_{\mathrm{TO}})/I_*$ is used to reflect the degree of crystallinity. Smaller FWHM values for the GaSb LO and TO modes and higher $(I_{\mathrm{LO}} + I_{\mathrm{TO}})/I_*$ values indicate better crystallinity. As shown in Fig. 2 and Table 1, the crystallinity of GaSb/quartz diminished with increasing growth rate. The crystallinity of GaSb/quartz was initially improved by Bi doping (x = 0.011 and 0.013), although it drastically deteriorated at x = 0.032. The LO and TO modes of GaSb shifted to lower

wavenumber with decreasing crystallinity. For GaSb/PI and $GaSb_{1-x}Bi_x$/PI, smaller values of $(I_{LO} + I_{TO})/I_*$ and larger shifts to lower wavenumber were observed compared with GaSb/quartz. These were attributable to reduced surface migration of the source materials on the activated PI film surface due to reverse sputtering. The crystallinity of GaSb/PI slightly improved with decreasing growth rate and further improvement of the crystallinity was observed upon Bi doping. In particular, the peak intensity of the GaSb TO mode and the $(I_{LO} + I_{TO})/I_*$ value were significantly increased at $x = 0.032$.

The XRD patterns and Raman spectra indicate that the crystallinity of the GaSb thin films was improved by Bi doping (Figs. 1 and 2). Good crystallinity for $GaSb_{1-x}Bi_x$/PI was obtained at $x = 0.032$. By contrast, the crystallinity of $GaSb_{1-x}Bi_x$/quartz deteriorated at $x = 0.032$ with increased surface roughness. Bi clusters were formed in $GaSb_{0.968}Bi_{0.032}$/quartz but not in $GaSb_{0.968}Bi_{0.032}$/PI because the surface migration of Bi atoms was insufficient for the generation of Bi clusters on the PI films. Clabel et al. reported that abnormal growth occurs because of the surface energy difference between normal and abnormal grains [29]. Therefore, the deterioration of crystallinity observed for $GaSb_{0.968}Bi_{0.032}$/quartz was ascribed to abnormal growth caused by the surface energy difference between the GaSb grains and Bi clusters.

Stacking-fault probabilities of GaSb/quartz and $GaSb_{1-x}Bi_x$/quartz

As described above, abnormal growth occurred at $x = 0.032$ with the formation of Bi clusters during the growth of $GaSb_{1-x}Bi_x$/quartz (Figs. 1 and 2). Stacking faults were speculated to be the structural defect and the structural changes in $GaSb_{1-x}Bi_x$/quartz due to the abnormal growth were analyzed. In the case of defect- and strain-free polycrystalline thin films, the plot of the lattice parameter against the diffractometer function $f(\theta)$ $(= \cos\theta\cot\theta)$ is linear. The following equation considering strain and stacking faults has been used for analyzing face-centered cubic metals [30, 31], and we also demonstrated that this analysis method is suitable for compound semiconductor thin films with a zinc-blende structure [21]:

$$a_{HKL} = a_0 + mf(\theta_{HKL}) + a_0\varepsilon_{(hkl)}^{zz} + a_0\left(G_{HKL} + \varepsilon_{(hkl)}^{\mathrm{SF}}J_{HKL}\right)\alpha_{(hkl)}^{\mathrm{SF}}, \quad (1)$$

where HKL is defined as integer multiples of the Miller indices (hkl), a_{HKL} is the lattice parameter corresponding to the diffraction angle θ_{HKL} in the XRD pattern, a_0 is the lattice constant (GaSb: 6.096 Å), m is a constant, $\varepsilon_{(hkl)}^{zz}$ is the strain vertical to the substrate due to the difference in thermal expansion coefficients between the substrate and the (hkl)-oriented crystal grains in the polycrystalline thin film, and $\varepsilon_{(hkl)}^{\mathrm{SF}}$ is fractional change in interplanar spacing. $\alpha_{(hkl)}^{\mathrm{SF}}$ is the net stacking-fault probability as

follows:

$$\alpha_{(hkl)}^{\mathrm{SF}} = \alpha_{(hkl)}^{\mathrm{ISF}} - \alpha_{(hkl)}^{\mathrm{ESF}}, \quad (2)$$

where $\alpha_{(hkl)}^{\mathrm{ISF}}$ and $\alpha_{(hkl)}^{\mathrm{ESF}}$ are the intrinsic and extrinsic stacking-fault probabilities, respectively.

Figure 3a, 3b and 3c shows plots of a_{HKL} against $f(\theta)$, where the solid lines represent $a_{HKL} = a_0 + mf(\theta_{HKL})$. Because m is defined for the defect- and strain-free states, it should be determined using thin films with good crystallinity. Thus, m (= 0.00091) was obtained by fitting the a_{HKL} values for GaSb/quartz grown at 17.6 nm/min (open circles in Fig. 3c) using the least-squares method; this sample exhibited strong (111) diffraction intensity in the XRD pattern and small FWHM values for the LO and TO modes of GaSb in the Raman spectrum. The deviations of a_{HKL} from the linear relation were smaller at x = 0.011 and 0.013 (Fig. 3a and 3b). By contrast, the values of a_{HKL} deviated from the linear relation at x = 0.032 except for the (111), (222), and (333) orientations as shown in Fig. 3c. Cross-sectional bright field TEM images of GaSb/quartz and $GaSb_{0.968}Bi_{0.032}$/quartz are shown in Fig. 3d and Fig. 3e, respectively. These correspond to Fig. 3c. The surface of $GaSb_{0.968}Bi_{0.032}$/quartz became rougher due to the abnormal growth (see the microscopy image in Fig. 3): TEM observation of $GaSb_{0.968}Bi_{0.032}$/quartz was performed at the position indicated by an arrow in the

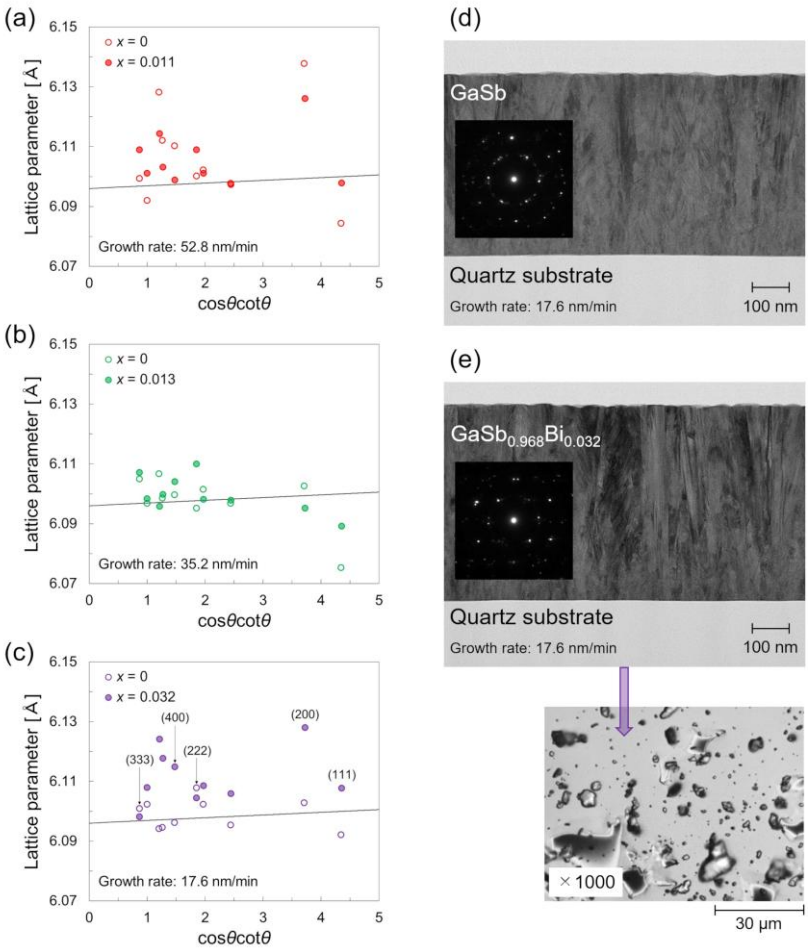

Fig. 3. Lattice parameters at various growth rates and Bi contents x as a function of $\cos\theta\cot\theta$: (a) growth rate = 52.8 nm/min, x = 0.011, (b) growth rate = 35.2 nm/min, x = 0.013, and (c) growth rate = 17.6 nm/min, x = 0.032. The lattice parameters for GaSb/quartz and $GaSb_{1-x}Bi_x$/quartz are indicated by open circles and closed circles, respectively. Cross-sectional bright field TEM images and selected area diffraction patterns of (d) GaSb/quartz and (e) $GaSb_{0.968}Bi_{0.032}$/quartz at the position indicated by an arrow in the microscopy image: the growth rate of these thin films was 17.6 nm/min. The inset microscopy image shows the surface morphology of $GaSb_{0.968}Bi_{0.032}$/quartz.

microcopy image. Although stacking faults were not identified, there were slightly more

defect structures in $GaSb_{0.968}Bi_{0.032}$/quartz (Fig. 3e) than in GaSb/quartz (Fig. 3d).

For the abnormal growth originating from Bi cluster formation, the changes in $\alpha^{\mathrm{SF}}_{(hkl)}$ and $\varepsilon^{\mathrm{SF}}_{(hkl)}$ were analyzed for the (100) and (111) orientations. As discussed with respect to the diffraction peak shifts in the XRD patterns, $\varepsilon^{zz}_{(hkl)}$ was zero for the thin films grown on quartz substrates. Hence, Δa_{HKL}, the deviation of a_{HKL} from the linear relation, can be expressed as follows:

$$\Delta a_{HKL} = a_{HKL} - a_0 - mf(\theta_{HKL}) = a_0\left(G_{HKL} + \varepsilon^{\mathrm{SF}}_{(hkl)} J_{HKL}\right)\alpha^{\mathrm{SF}}_{(hkl)}, \quad (3)$$

where G_{HKL} and J_{HKL} are constants depending on the diffraction planes. $\alpha^{\mathrm{SF}}_{(100)}$ and $\varepsilon^{\mathrm{SF}}_{(100)}$ can be estimated by solving the following simultaneous equations:

$$\Delta a_{200} = a_0\left(G_{200} + \varepsilon^{\mathrm{SF}}_{(100)} J_{200}\right)\alpha^{\mathrm{SF}}_{(100)}, \quad (4)$$

$$\Delta a_{400} = a_0\left(G_{400} + \varepsilon^{\mathrm{SF}}_{(100)} J_{400}\right)\alpha^{\mathrm{SF}}_{(100)}, \quad (5)$$

where G_{200} = 0.0689, G_{400} = −0.0345, and J_{200} = J_{400} = −0.167 [32]. In the same manner, $\alpha^{\mathrm{SF}}_{(111)}$ and $\varepsilon^{\mathrm{SF}}_{(111)}$ can be calculated by solving the simultaneous equations for Δa_{111} and Δa_{222}. Here, G_{111} = −0.0345, G_{222} = 0.0172, and J_{200} = J_{400} = 0.209 [32]. Figure 4 shows a comparison of the $\alpha^{\mathrm{SF}}_{(hkl)}$ and $\varepsilon^{\mathrm{SF}}_{(hkl)}$ values for GaSb/quartz and $GaSb_{0.968}Bi_{0.032}$/quartz grown at 17.6 nm/min. Upon Bi doping of GaSb/quartz, $\alpha^{\mathrm{SF}}_{(111)}$ decreased while $\alpha^{\mathrm{SF}}_{(100)}$ increased. In addition, $\varepsilon^{\mathrm{SF}}_{(111)}$ and $\varepsilon^{\mathrm{SF}}_{(100)}$ increased in the negative direction, where a negative $\varepsilon^{\mathrm{SF}}_{(hkl)}$ corresponds to shrinkage of the interplanar

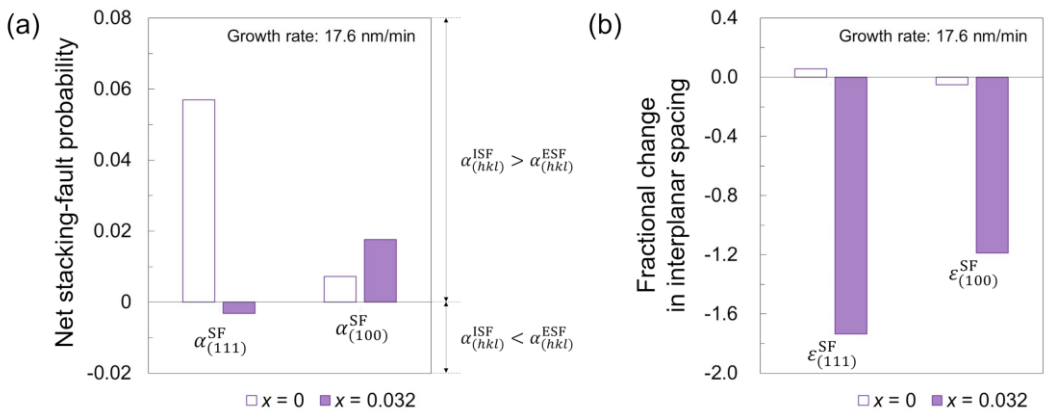

Fig. 4. Estimated (a) net stacking-fault probability $\alpha^{SF}_{(hkl)}$ and (b) fractional change in interplanar spacing $\varepsilon^{SF}_{(hkl)}$ at various (hkl) and Bi contents x.

spacing at the stacking fault. As noted above, the diffraction peaks of $GaSb_{0.968}Bi_{0.032}$/quartz shifted to lower angles in the XRD pattern, indicating the presence of compressive strain that manifested as shrinkage at the stacking faults. Consequently, these results reveal that the structural defects generated by the formation of Bi clusters increased at the crystal planes except for the (111) orientation and induced compressive strain in the $GaSb_{0.968}Bi_{0.032}$/quartz.

Grain size and electrical properties

Figure 5 presents the grain sizes for the GaSb and $GaSb_{1-x}Bi_x$ thin films grown on quartz substrates and PI films estimated by analysis of the XRD patterns. Insets (i) and (ii) show AFM images of $GaSb_{0.989}Bi_{0.011}$/quartz and GaSb/quartz grown at 52.8 nm/min,

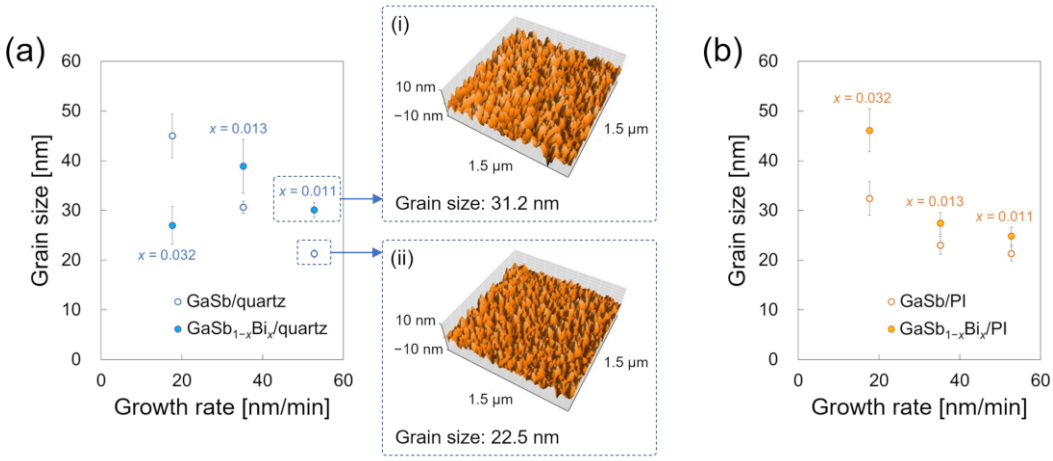

Fig. 5. Grain sizes of GaSb and $GaSb_{1-x}Bi_x$ thin films grown on (a) quartz substrates and (b) PI films. Insets (i) and (ii) show AFM images of GaSb/quartz and $GaSb_{0.989}Bi_{0.011}$/quartz grown at 52.8 nm/min.

which exhibited low grain size dispersion. The AFM images confirmed the accuracy of the grain sizes estimated from the XRD results. The grain size was dependent on the crystallinity as evaluated by XRD and Raman spectroscopy, and a large grain size was observed for the thin films with good crystallinity. With the exception of $GaSb_{0.968}Bi_{0.032}$/quartz, where the abnormal growth due to the formation of Bi clusters reduced the grain size, the grain sizes of the $GaSb_{1-x}Bi_x$ thin films increased upon Bi doping. These increases in grain size indicate that the growth of the GaSb thin films was assisted by doping with Bi.

Figure 6 shows the electrical properties of the obtained thin films, which were determined by Hall effect measurements at room temperature. As shown in Figs. 5 and

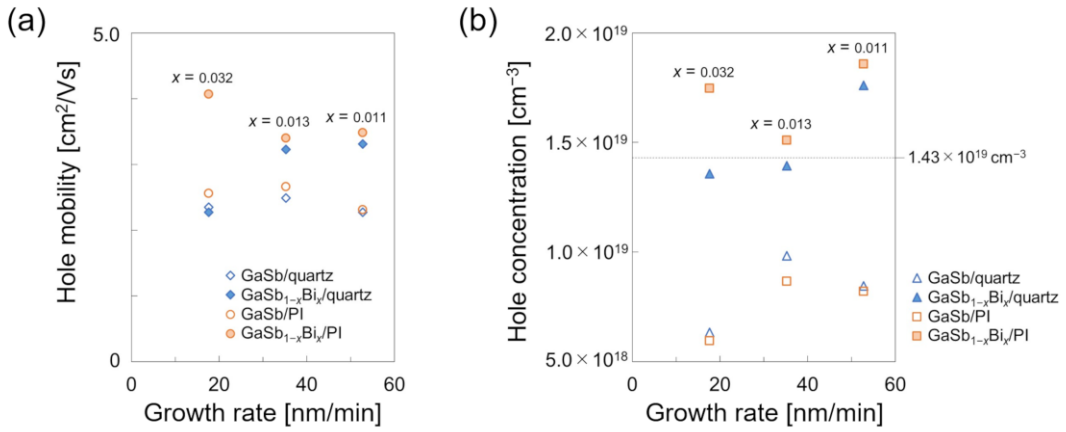

Fig. 6. (a) Hole mobilities and (b) hole concentrations of GaSb and $GaSb_{1-x}Bi_x$ thin films for various substrates, growth rates, and Bi contents x. Open and closed symbols correspond to GaSb and $GaSb_{1-x}Bi_x$ thin films, respectively.

6a, the change in hole mobility μ_h mostly followed the change in grain size because grain boundary scattering is the dominant carrier scattering mechanism in polycrystalline thin films. However, μ_h of GaSb/quartz and GaSb/PI decreased at the growth rate of 17.6 nm/min even though their grain sizes increased with decreasing growth rate. This is ascribed to the purity of the $Ga_{0.497}Sb_{0.503}$ target. As mentioned in the Materials and methods, the growth rates of 17.6, 35.2, or 52.8 nm/min were controlled by varying the number of sputtering targets from one to three. The Fe impurity concentration was 0.0040 wt% in the $Ga_{0.497}Sb_{0.503}$ target used for the GaSb thin films grown at 17.6 nm/min, while those of the other two $Ga_{0.497}Sb_{0.503}$ targets added for higher growth rates were 0.0006 wt%. Hence, higher levels of Fe impurities were inferred to be present in the GaSb thin

films grown at 17.6 nm/min in comparison with those grown at higher growth rates. In III-V compound semiconductors, Fe impurities form deep impurity levels and act as hole traps [33, 34]. Thus, the decreases in μ_{h}, which were observed in GaSb thin films grown at 17.6 nm/min, can be attributed to Fe impurities. On the other hand, the hole concentration n_{h} increased upon Bi doping as shown in Fig. 6b. GaSb exhibits p-type conductivity irrespective of the growth method owing to the formation of Ga antisites ($\mathrm{Ga_{Sb}}$), which serve as acceptors with the lowest defect formation energy [35, 36]. For this reason, the increase in $\mathrm{Ga_{Sb}}$ concentration caused by the increased crystallization degree upon Bi doping was considered to be responsible for the increase in n_{h}. We previously reported that p-type GaSb with an n_{h} value exceeding approximately 1.43×10^{19} cm^{-3} is a degenerate semiconductor by solving the following equation [14]:

$$n_{\mathrm{h}}(T) = N_{\mathrm{V}}(T)\mathscr{F}_{1/2}(\eta_{\mathrm{h}}), \tag{6}$$

where $N_{\mathrm{V}}(T)$ is the effective density of state of the valence band and $\mathcal{F}_{1/2}(\eta_{\mathrm{h}})$ is the normalized Fermi–Dirac integral as follows:

$$\mathscr{F}_{1/2}(\eta_{\mathrm{h}}) = \frac{2}{\sqrt{\pi}}\int_0^{\infty}\frac{\varepsilon^{1/2}}{1+\exp(\varepsilon-\eta_{\mathrm{h}})}d\varepsilon. \tag{7}$$

Here, η_{h} is the reduced Fermi level for holes and ε is the reduced hole energy. Accordingly, $\mathrm{GaSb_{0.989}Bi_{0.011}}$/quartz and $\mathrm{GaSb_{1-x}Bi_x}$/PI ($x = 0.011$, 0.013, and 0.032) were inferred to be degenerate because their n_{h} values were greater than 1.43×10^{19} cm^{-3}

(Fig. 6). The acceptor levels of Ga_{Sb} with a high concentration formed the acceptor band and the Fermi level was located in the valence band.

Elution tests of GaSb/PI and $GaSb_{0.968}Bi_{0.032}$/PI

Flexible materials have been applied to biomedical and environmental devices [37, 38]. Although GaSb has suitable properties for biomedical sensors and solar cells [8, 39], Sb is a toxic element [40]. Thus, improving the chemical stability of flexible GaSb-based thin films would enhance their safety for use in biomedical devices and reduce the environmental burden. We previously performed elution tests of GaSb/quartz under simulated physiological conditions, which revealed minimal elution in pH 5 buffer and substantial elution in pH 9 buffer [8]. Accordingly, in the present work the influence of Bi doping on the elution of Ga and Sb from GaSb/PI in pH 9 buffer was examined.

Figure 7a shows the amounts of Ga and Sb eluted from GaSb/PI and $GaSb_{0.968}Bi_{0.032}$/PI grown at 17.6 nm/min during immersion in pH 9 buffer for 48 h. The results revealed that almost the same amount of Ga was eluted from GaSb/PI and $GaSb_{0.968}Bi_{0.032}$/PI, whereas a larger amount of Sb was eluted from GaSb/PI than from $GaSb_{0.968}Bi_{0.032}$/PI. Insets (i) and (ii) present photographs of the surfaces of GaSb/PI and $GaSb_{0.968}Bi_{0.032}$/PI, respectively, after performing the elution tests for 48 h. No residue

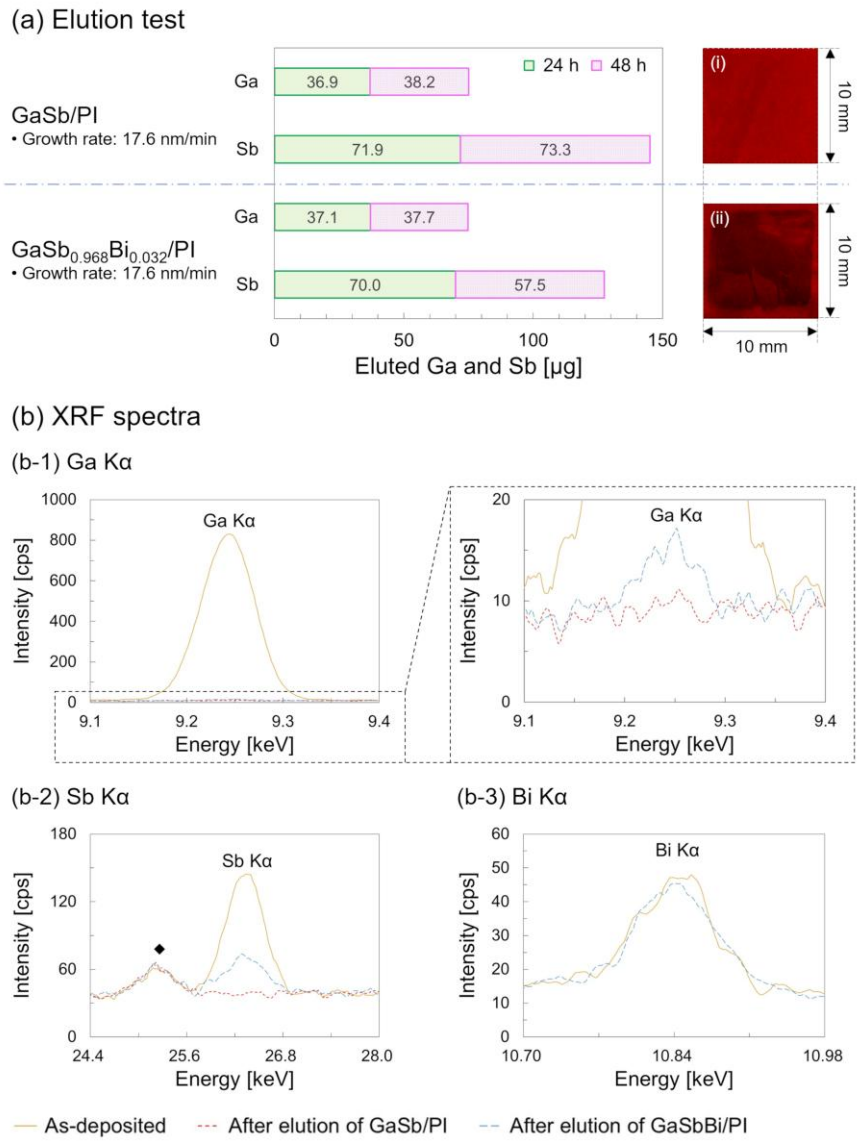

Fig. 7. (a) Total amounts of Ga and Sb eluted from GaSb/PI and $GaSb_{0.968}Bi_{0.032}$/PI. Insets (i) and (ii) show the surfaces of GaSb/PI and $GaSb_{0.968}Bi_{0.032}$/PI, respectively, after performing the elution tests for 48 h. (b) XRF spectra before and after immersion in pH 9 buffer for 48 h: (b-1) Ga Kα, (b-2) Sb Kα, and (b-3) Bi Kα. The solid, dotted, and broken lines represent the spectra before elution (as-deposited) and after elution for GaSb/PI and $GaSb_{0.968}Bi_{0.032}$/PI, respectively.

was visible on the GaSb/PI surface, whereas a residue of uneven thickness was observed

on the $GaSb_{0.968}Bi_{0.032}$/PI surface. The residue remaining on $GaSb_{0.968}Bi_{0.032}$/PI was thus considered to be Sb. Figure 7b shows the XRF spectra of GaSb/PI and $GaSb_{0.968}Bi_{0.032}$/PI before and after the elution tests. The as-deposited spectra are only shown for $GaSb_{0.968}Bi_{0.032}$/PI because the Ga Kα and Sb Kα spectra of the as-deposited samples of GaSb/PI and $GaSb_{0.968}Bi_{0.032}$/PI prior to elution were almost identical. The incident X-rays were focused to a 1-mm-diameter spot and the XRF spectra were measured at the center of the thin film. The peak indicated by a black diamond (◆) in Fig. 7b-2 corresponds to a Sn Kα signal originating from the sample holder. After the elution tests, no Ga Kα or Sb Kα signals could be detected for GaSb/PI, whereas Ga Kα, Sb Kα, and Bi Kα signals were observed for $GaSb_{0.968}Bi_{0.032}$/PI. The peak intensities for Ga Kα and Sb Kα had decreased to 2% and 51%, respectively, of those for the as-deposited sample, while the peak intensity for Bi Kα was unchanged. These results suggest that Bi doping is effective for reducing Sb elution from $GaSb_{0.968}Bi_{0.032}$/PI, which may be attributable to an anchoring effect [41, 42].

Conclusion

In this work, we deposited GaSb and $GaSb_{1-x}Bi_x$ (x = 0.011, 0.013, or 0.032) thin films on quartz substrates and PI films by multi-cathode RF magnetron sputtering to

investigate the effects of dilute Bi doping. Good crystallinity was observed for GaSb/quartz compared with GaSb/PI. Except for $GaSb_{0.968}Bi_{0.032}$/quartz, Bi assisted the growth of the GaSb thin films: structural disorder and defects were decreased, and the grain size was increased. In particular, the crystallinity of $GaSb_{0.968}Bi_{0.032}$/PI was significantly improved. Bi clusters were not generated on PI films due to the insufficient surface migration of Bi atoms. By contrast, the crystallinity of $GaSb_{0.968}Bi_{0.032}$/quartz was deteriorated by abnormal growth due to Bi cluster formation. Furthermore, elution tests of GaSb/PI and $GaSb_{0.968}Bi_{0.032}$/PI demonstrated that Bi doping was effective for reducing the elution of highly toxic Sb. This study is the first to deposit GaSb and $GaSb_{1-x}Bi_x$ by sputtering at low temperature and to reveal the effects of dilute Bi doping on the crystallinity and chemical stability of sputter deposited GaSb thin films. These findings are anticipated to prove useful for the development of biomedical and environmental devices using flexible Sb-based materials.

Acknowledgements

This work was supported by Japan Society for the Promotion of Science (JSPS) a Grant-in-Aid for Scientific Research (B) (grant number 21H03212) to Junko Fujihara.

Author contributions

Conceptualization: Naoki Nishimoto; Investigation and data curation: Naoki Nishimoto, Junko Fujihara; Formal analysis: Naoki Nishimoto; Funding acquisition: Junko Fujihara; Writing – original draft preparation: Naoki Nishimoto; Writing – review and editing: Naoki Nishimoto, Junko Fujihara

Declarations

Conflict of interest

The authors declare that they have no conflict of interest.

Data and code availability

Not applicable.

Supplementary information

Not applicable.

Ethical approval

Not applicable.

References

[1] Schaefer ST, Gao S, Webster PT, Kosireddy RR, Johnson SR (2020) Absorption edge characteristics of GaAs, GaSb, InAs, and InSb. J Appl Phys 127:165705. doi: 10.1063/5.0003001

[2] Stephan S, Frederic D, Markus-Christian A (2016) Novel InP- and GaSb-based light sources for the near to far infrared. Semicond Sci Technol 31:113005. doi: 10.1088/0268-1242/31/11/113005

[3] Rogalski A, Martyniuk P, Kopytko M (2017) InAs/GaSb type-II superlattice infrared detectors: Future prospect. Appl Phys Rev 4:031304 doi: 10.1063/1.4999077

[4] Manzo DJ, Bolzan CA, Marcos A, de Andrade H, Schoffen JR, Giulian R (2019) Structural and compositional analysis of GaSb nanoforms obtained by ion irradiation of sputtered films. Thin Solid Films 687:137447. doi: 10.1016/j.tsf.2019.137447

[5] Gupta P, Kim Y, Ilm J, Kang G, Urbas AM, Kim K (2021) Enhancing the Efficiency of GaSb Photovoltaic Cell Using Thin-Film Multiscale Haze and Radiative Cooling. ACS Appl Energy Mater 4:9304–9314. doi: 10.1021/acsaem.1c01536

[6] Montealegre DA, Schrock KN, Walhof AC, Muellerleile AM, Prineas JP (2021) High-power mid-wave infrared LED using W-superlattices and texture surfaces. Appl Phys Lett 118:071105. doi: 10.1063/5.0039269

[7] Asirvatham J, Luong MA, Baraik K, Ganguli T, Claverie A, Kanjilal A (2022) Revealing the Impact of Prestructural Ordering in GaSb Thin Films. J Phys Chem C 126:15405–15414. doi: 10.1021/acs.jpcc.2c02893

[8] Nishimoto N, Fujihara J (2017) Biocompatibility of GaSb thin films grown by RF magnetron sputtering. Appl Surf Sci 409:375–380. doi: 10.1016/j.apsusc.2017.03.099

[9] Goncalves LM, Alpuim P, Min G, Rowe DM, Couto C, Correia JH (2008) Optimization of Bi_2Te_3 and Sb_2Te_3 thin films deposited by co-evaporation on polyimide for thermoelectric applications. Vacuum 82:1499–1502. doi: 10.1016/j.vacuum.2008.03.076

[10] Prepelita P, Medianu R, Sbarcea B, Garoi F, Filipescu M (2010) The influence of using different substrates on the structural and optical characteristics of ZnO thin films. Appl Surf Sci 256:1807–1811. doi: 10.1016/j.apsusc.2009.10.011

[11] Chen CH, Chiu CT, Su LC, Huang KT, Shin J, Stringfellow GB (1993) Tertiaybutyldimethylantimony for GaSb growth. J Electron Mater 22:87–91. doi: 10.1007/BF02665728

[12] Akahane K, Yamamoto N, Gozu S, Ohtani N (2004) Heteroepitaxial growth of GaSb on Si(001) substrates. J Cryst Growth 264:21–25. doi: 10.1016/j.jcrysgro.2003.12.041

[13] Wang CC, McFarlane SH (1972) Epitaxial growth and characterization of GaP on insulating substrates. J Cryst Growth 13-14:262–267. doi: 10.1016/0022-0248(72)90166-2

[14] Nishimoto N, Fujihara J (2017) Control of the conduction mechanism via the formation of native defects in RF-magnetron-sputtered GaSb thin films on Ge(100) substrates. J Cryst Growth 468:732–736. doi: 10.1016/j.jcrysgro.2016.11.082

[15] Nishimoto N, Fujihara J, Kitahara K (2015) Evaluation of ZnO-MgO Mixed Thin Films Grown by Metal-Organic Decomposition. e-J Surf Sci Nanotech 13:185–189. doi: 10.1380/ejssnt.2015.185

[16] Peksu E, Karaagac H (2018) Doping and annealing effects on structural, electrical and optical properties of tin-doped ZnO thin films. J Alloys Compd 764:616–625. doi: 10.1016/j.jallcom.2018.06.101

[17] Gougousi T (2021) Low-Temperature Dopant-Assisted Crystallization of HfO_2 Thin Films. Cryst Growth Des 21:6411–6416. doi: 10.1021/acs.cgd.1c00875

[18] Mohmad AR, Bastiman F, Hunter CJ, Ng JS, Sweeney SJ, David JPR (2011) The effect of Bi composition to the optical quality of $GaAs_{1-x}Bi_x$. Appl Phys Lett 99:042107. doi: 10.1063/1.3617461

[19] Greene JE, Wickersham CE (1976) Structural and electrical characteristics of InSb

thin films grown by rf sputtering. J Appl Phys 47:3630. doi: 10.1063/1.323170

[20] Michel E, Singh G, Slivken S, Besikci C, Bove P, Ferguson I, Razeghi M (1994) Molecular beam epitaxy growh of high quality InSb. Appl Phys Lett 65:3338. doi: 10.1063/1.112384

[21] Nishimoto N, Fujihara J (2022) Improvement of the structural properties and environmental stability of flexible InSb thin films by dopant-assisted crystallization. Appl Phys A 128:550. doi: 10.1007/s00339-022-05694-8

[22] Fujihara J, Nishimoto N (2020) Total antimony analysis by hydride generation-microwave plasma-atomic emission spectroscopy with applications. Microchem J 157:104992. doi: 10.1016/j.microc.2020.104992

[23] Murmu PP, Levenur J, Storey JG, Kennedy J (2021) Effect of surface nanopatterning on the thermoelectric properties of bismuth antimony telluride films. Mater Today Proc 36:416–420. doi: 10.1016/j.matpr.2020.04.752

[24] Hicyilmaz AS, Bedeloglu AC (2021) Applications of polyimide coatings: a review. SN Appl Sci 3:363. doi: 10.1007/s42452-021-04362-5

[25] Cheetham KJ, Carrington PJ, Krier A, Patel II, Martin FL (2012) Raman spectroscopy of pentanary GaInAsSbP narrow gap alloys lattice matched to InAs and GaSb. Semicond Sci Technol 27:015004. doi: 10.1088/0268-1242/27/1/015004

[26] Zhou X, Guo W, Perez-Bergquist AG, Wei Q, Chen Y, Sun K, Wang L (2011) Optical Properties of GaSb Nanofibers. Nanoscale Res Lett 6:6. doi: 10.1007/s11671-010-9739-2

[27] Mishra P, Kumari S (2022) Investigation of Be doped GaSb with varying hole concentration using single magnetic field Hall measurement and Raman spectroscopy. J Phys Chem Solids 163:110570. doi: 10.1016/j.jpcs.2021.110570

[28] Klein PB, Chang RK (1976) Comparison of second-order Raman scattering measurements with a phonon density-of-states calculation in GaSb. Phys Rev B 14:2498–2502. doi: 10.1103/PhysRevB.14.2498

[29] Clabel HJL, Nazrin SN, Lozano CG, Pereira da Silva M, Siu Li M, Marega E (2021) Activation energy and its fluctuations at grain boundaries of Er^{3+}:$BaTiO_3$ perovskite thin films: Effect of doping concentration and annealing temperature. Vacuum 194:110562. doi: 10.1016/j.vacuum.2021.110562

[30] Wagner CNJ, Tetelman AS (1962) Diffraction from Layer Faults in bcc and fcc Structures. J Appl Phys 33:3080–3086. doi: 10.1063/1.1728571

[31] Reed RP, Schramm RE (1974) Relationship between stacking-fault energy and X-ray measurements of stacking-fault probability and microstrain. J Appl Phys 45:4705. doi: 10.1063/1.1663122

[32] Adler RPI, Wagner CNJ (1970) X-Ray Diffraction Study of a Bulk, Polycrystalline Ag-9 At. Pct Sn Alloy Deformed in Compression. Metall Mater Trans B 1:2791–2797. doi: 10.1007/BF03037816

[33] Shockley W, Read WT (1952) Statistics of the Recombinations of Holes and Electrons. Phys Rev 87:835–842. doi: 10.1103/PhysRev.87.835

[34] Sze SM, Irvin JC (1968) Resistivity, mobility and impurity levels in GaAs, Ge, and Si at 300°K. Solid State Electron 11:599–602. doi: 10.1016/0038-1101(68)90012-9

[35] Dutta PS, Bhat HL, Kumar V (1997) The physics and technology of gallium antimonide: An emerging optoelectronic material. J Appl Phys 81:5821–5870. doi: 10.1063/1.365356

[36] Virkkala V, Havu V, Tuomisto F, Puska MJ (2012) Native point defect energetics in GaSb: Enabling *p*-type conductivity of undoped GaSb. Phys Rev B 86:144101. doi: 10.1103/PhysRevB.86.144101

[37] Tang G, Yan F (2021) Recent progress of flexible perovskite solar cells. Nano Today 39:101155. doi: 10.1016/j.nantod.2021.101155

[38] Sreenilayam SP, Ahad IU, Nicolosi V, Brabazon D (2021) MXene materials based printed flexible devices for healthcare, biomedical and energy storage applications. Mater Today 43:99–131. doi: 10.1016/j.mattod.2020.10.025

[39] Renteria EJ, Mansoori A, Addamane SJ, Shima DM, Hains CP, Balakrishnan G (2016) Development of thin film metamorphic GaSb cells by epitaxial lift-off from GaAs substrates. 2016 IEEE 43rd Photovoltaic Specialists Conference (PVSC) 2310–2312. doi: 10.1109/PVSC.2016.7750049

[40] Boreiko CJ, Rossman TG (2020) Antimony and its compounds: Health impacts related to pulmonary toxicity, cancer, and genotoxicity. Toxicol Appl Pharmacol 403:115156. doi: 10.1016/j.taap.2020.115156

[41] Jeon BJ, Ko H, Hyun J, Byun D, Lee JK (2006) The effect of direct current bias on the characteristics of Cu/C:H composite thin films on poly ethylene terephthalate film prepared by electron cyclotron resonance-metal organic chemical vapor deposition. Thin Solid Films 496:395–401. doi: 10.1016/j.tsf.2005.09.095

[42] Hu S, Wang Y, Wang W, Han Y, Fan Q, Feng X, Xu Q, Zhu J (2015) Ag Nanoparticles on Reducible CeO_2(111) Thin Films: Effect of Thickness and Stoichiometry of Ceria. J Phys Chem C 119:3579–3588. doi: 10.1021/jp511691p

Table 1. Numerical data obtained from curve-fitting analysis of the Raman spectra: (a) GaSb/quartz, (b) $GaSb_{1-x}Bi_x$/quartz, (c) GaSb/PI, and (d) $GaSb_{1-x}Bi_x$/PI. $GaSb_{0.968}Bi_{0.032}$/quartz was measured at two positions, as indicated by the letters (i) and (ii) in the inset microscopy image shown in Fig. 2.

Quartz substrate						
Film composition			Growth rate [nm/min]	FWHM [cm^{-1}] LO mode	TO mode	$(I_{LO} + I_{TO})/I_*$
(a)	GaSb		52.8	7.7	9.6	1.68
			35.2	7.1	9.2	2.68
			17.6	6.4	7.8	4.53
(b)	$GaSb_{1-x}Bi_x$	$x = 0.011$	52.8	6.8	8.6	3.85
		$x = 0.013$	35.2	6.5	8.5	5.03
		$x = 0.032$, (i)	17.6	6.6	8.7	1.96
		$x = 0.032$, (ii)		7.4	9.0	0.96
PI film						
Film composition			Growth rate [nm/min]	FWHM [cm^{-1}] LO mode	TO mode	$(I_{LO} + I_{TO})/I_*$
(c)	GaSb		52.8	10.1	9.8	0.36
			35.2	9.5	9.2	0.39
			17.6	9.0	9.0	0.45
(d)	$GaSb_{1-x}Bi_x$	$x = 0.011$	52.8	7.7	9.7	0.44
		$x = 0.013$	35.2	7.6	9.0	0.49
		$x = 0.032$	17.6	6.7	6.8	2.03

I_{LO} and I_{TO} are the peak intensities of the LO and TO modes of GaSb, respectively. I_* is the sum of two peak intensities originating from structural disorder as shown in Fig. 2 (region *).